nature COMMUNICATIONS

ARTICLE

Received 25 Nov 2014 | Accepted 28 Mar 2015 | Published 12 May 2015

DOI: 10.1038/ncomms8070 OPEN

# High-speed multiple-mode mass-sensing resolves dynamic nanoscale mass distributions

Selim Olcum[1,*], Nathan Cermak[2,*], Steven C. Wasserman[3] & Scott R. Manalis[1,2,3,4]

Simultaneously measuring multiple eigenmode frequencies of nanomechanical resonators can determine the position and mass of surface-adsorbed proteins, and could ultimately reveal the mass tomography of nanoscale analytes. However, existing measurement techniques are slow (<1 Hz bandwidth), limiting throughput and preventing use with resonators generating fast transient signals. Here we develop a general platform for independently and simultaneously oscillating multiple modes of mechanical resonators, enabling frequency measurements that can precisely track fast transient signals within a user-defined bandwidth that exceeds 500 Hz. We use this enhanced bandwidth to resolve signals from multiple nanoparticles flowing simultaneously through a suspended nanochannel resonator and show that four resonant modes are sufficient for determining their individual position and mass with an accuracy near 150 nm and 40 attograms throughout their 150-ms transit. We envision that our method can be readily extended to other systems to increase bandwidth, number of modes, or number of resonators.

[1] Koch Institute for Integrative Cancer Research, Massachusetts Institute of Technology, Cambridge, Massachusetts 02139, USA. [2] Program in Computational and Systems Biology, Massachusetts Institute of Technology, Cambridge, Massachusetts 02139, USA. [3] Department of Biological Engineering, Massachusetts Institute of Technology, Cambridge, Massachusetts 02139, USA. [4] Department of Mechanical Engineering, Massachusetts Institute of Technology, Cambridge, Massachusetts 02139, USA. * These authors contributed equally to this work. Correspondence and requests for materials should be addressed to S.R.M. (email: srm@mit.edu).

High-quality factors[1], miniature sizes and small force constants of micro- and nanomechanical resonators have enabled extremely sensitive detection of weak forces[2], single-molecule interactions[3,4], single-electron spin[5,6], temperature [7] or mass perturbations[8,9]. Most mass sensors detect changes in resonant frequency, a method that has facilitated many exquisite measurements including the weight of single molecules[9], proteins[10], exosomes[11], nanoparticles[11,12], cells[13–16] and various accreted chemical analytes[17]. Although these measurements typically exploit perturbations in the fundamental mode frequency, the combined information from multiple modes can yield improved stability[18] or additional characteristics of analytes. For example, Dohn *et al.*[19] used multimode measurements to determine the mass and position of attached beads on a microcantilever. Similarly, Hanay *et al.*[10] measured the mass and position of individual proteins adsorbed on a nanomechanical resonator by measuring the frequency of its first two modes. Beyond mass and position of point masses, multimode measurements have recently been proposed for characterizing continuous mass distributions with atomic-scale resolution[20], which would be a powerful approach for characterizing biological and synthetic micro- and nanostructures.

However, current systems for multimode frequency measurement are slow, with measurement bandwidths below 1 Hz. Although the speed of open-loop frequency measurements (either thermally or externally driven) are limited by the resonator amplitude timescale[21], most multimode measurements to date have been performed this way[19,20,22–26]. Existing closed-loop systems also have limited bandwidths (below 1 Hz)[10]. Narrow measurement bandwidths limit throughput—for example, nanomechanical mass spectrometers must measure faster than the time interval between arrivals of individual particles. In addition, wide bandwidths are necessary for resonator sensors that generate fast frequency modulated signals.

Here we introduce a method for wide-bandwidth multimode frequency measurements while oscillating each resonance mode in closed-loop and apply it to measure rapidly changing nanoscale mass distributions. In contrast to previous research exploiting static particles adhered to the surface of a resonator in vacuum[10,19,22], we focus on multimode measurements of analytes in motion, while they flow through a suspended nanochannel resonator (SNR)—a vacuum-packaged microcantilever with an embedded fluidic channel[12] that can measure the masses of nanoparticles[11]. Here, we utilize a scalable system to simultaneously oscillate and track multiple modes of a 200-μm-long SNR in a wide bandwidth. As a demonstration, we track the first four modes to resolve the position and mass of nanoparticle pairs in close proximity as they quickly flow through the resonator. Resolving such closely spaced moving point masses is an important milestone for measuring mass distributions of analytes in solution with high throughput and high resolution.

## Results

**Oscillation scheme**. In comparison with open-loop techniques, closed-loop approaches in which the resonator is placed in a feedback loop provide wider measurement bandwidths[21]. Furthermore, higher oscillation amplitudes (below the onset of mechanical nonlinearity) lead to reduced frequency measurement noise[27]. For oscillating a single mode, the feedback path typically consists of a phase shift and gain, such that the resonator position signal is delayed, amplified and then fed back to excite the resonator[11,28]. This is straightforward to implement and ensures that the loop oscillation frequency nearly instantly follows the resonant frequency[21]. However, for multiple modes it does not allow the phase shift and vibration amplitude for each mode to be separately optimized—a critical requirement for minimizing frequency noise. In contrast, a dedicated phase-locked loop (PLL) in closed loop with each mode as depicted in Fig. 1a allows for setting the phase shift and oscillation amplitude independently.

While separate PLL feedback paths enable independent control over each resonance, they also affect the system dynamics. The ideal resonator-PLL system should track the corresponding resonant frequency as closely and quickly as possible. While direct feedback loops respond to perturbations much faster than the resonator's characteristic amplitude timescale (typically $\tau = 2Q/\omega_0$, where $Q$ and $\omega_0$ are the quality factor and the angular resonant frequency of the resonator) the case of PLL-mediated feedback[29–33] and its dynamics[34–36] have been less studied. Therefore, we first developed a Laplace domain model for the resonator-PLL system to understand and then tailor the closed-loop system dynamics.

**Controlling resonator—PLL system dynamics**. To model the resonator-PLL system, we first required the transfer function of the resonator's phase. We utilized the time-domain response of a driven harmonic oscillator excited on resonance until time zero and slightly off-resonance after time zero (see Supplementary Note 1). The step change in excitation frequency is conceptually equivalent to instantaneously changing the resonant frequency (for example, by mass adsorption). Approximating the resonator phase delay to be linear around its resonant frequency (Fig. 1b), the first-order Taylor series approximation of the phase term from the time-domain solution reveals that the resonator phase can be well approximated as a first-order low-pass filter in the Laplace domain (Fig. 1c and Supplementary Fig. 1), with a bandwidth equal to $1/\tau$. In the Laplace domain, the transfer function of the resonator phase is:

$$\Phi(s) = \frac{1}{\tau s + 1} \tag{1}$$

This is valid for frequency steps that are much smaller than $1/\tau$. Figure 1d shows the complete model of a generic resonator-PLL system and suggests that the quality factor of the resonator will substantially influence the loop dynamics especially at high modulation frequencies, demonstrated in Fig. 1e.

For high-precision frequency tracking at high speed, we want each mode's closed-loop transfer function to be maximally flat up to a desired bandwidth. Equating the resonator-PLL transfer function to a Butterworth low-pass filter of desired order and bandwidth yields direct expressions for the PLL parameters to achieve the desired response (Supplementary Note 3). Increasing the PLL order by introducing additional poles in the loop filter (Supplementary Fig. 2b) and using the corresponding parameters in Supplementary Table 1 sharpens the pass-band to stop-band transition (Supplementary Fig. 3). By exploiting this useful relationship, optimally configured resonator-PLL systems can be designed to minimize crosstalk between closely spaced resonant frequencies, such as those that occur in resonator arrays.

**Resonator—PLL system implementation**. For realization of a multiple-mode frequency-tracking system, we implemented a scalable array of 12 PLLs in a field-programmable gate array (FPGA) chip, using an architecture similar to other designs (see Methods)[37]. Since the mode frequencies of the SNR are not closely spaced, here we used second order, type 2 PLLs[38], which can be simplified to first-order low-pass filters when in closed loop with the resonator (first row of Supplementary Table 1 or ref. 34). The implementation of each PLL includes a phase-error

detector, a loop filter and a numerically controlled oscillator (see Methods and Supplementary Fig. 2c). Software-programmable parameters in the loop filter control the loop dynamics. To test our system implementation, we measured transfer functions of a PLL alone and a resonator-PLL system over a range of PLL parameters. Across all parameters tested, these transfer functions show excellent agreement with our model predictions for both PLL-only and resonator-PLL cases (see Supplementary Fig. 4 and Supplementary Note 4).

We then placed our PLL array in feedback with an SNR that is 200 μm long, 16 μm wide and 1.3 μm thick with an integrated channel that is 2 μm wide and 700 nm tall. The PLLs excite the resonator modes by driving a piezoceramic actuator seated underneath the chip and an optical lever detector measures the resonator deflection at the tip[11], which is fed back to the PLLs. The frequencies of the first four modes were 40.48, 249.1, 693.1 and 1,351 kHz, and their quality factors were between 3,500 and 8,000 (Fig. 2a). Beyond the fourth mode, our piezoceramic was not able to actuate the resonator with sufficient amplitude. We configured the closed-loop frequency response of each mode to behave as a first-order low-pass filter (Fig. 2b) by setting the loop parameters using Supplementary Table 1. The bandwidth for each mode was chosen to be wide enough for resolving particles with >100-ms-transit time and ranged from 150 to 500 Hz (see Supplementary Fig. 5 and Supplementary Note 5).

**Nanoparticle mass distribution measurements**. Next, we measured the resonant frequency signals of all four modes while a mixture of 100 and 150 nm gold nanoparticles flowed through the resonator (Fig. 2e). As particles typically took longer than 100 ms to transit the resonator, we averaged and downsampled the signals to a sampling rate of 642 Hz, yielding acquisition bandwidths between 150 and 285 Hz. We fit the resulting frequency signals to a model of a point loading on a cantilever[22] to obtain single particle mass and trajectory information (see Methods). The model assumed that the particle could be in any position at any time (that is, one free parameter for each time point) and that particle mass is constant during transit. The data systematically deviated from the model in that the magnitudes of frequency shift of modes two, three and four were smaller than predicted (Fig. 3a). Empirically, adding sensitivity-adjustment parameters for modes two through four significantly improved the fit (Fig. 3a, blue curves) and reduced the root-mean-square (RMS) error by 25% with only three additional degrees of freedom. An example of a best-fit particle trajectory is shown in Fig. 3b. The mean estimated sensitivity adjustment factors obtained by fitting 31 150-nm particles are shown in Fig. 3c. We are uncertain as to the origin of these deviations, although they are not attributable to undesired smoothing via insufficient bandwidth.

As a first step towards obtaining mass distributions within a microfluidic channel, we demonstrate the capability of our system

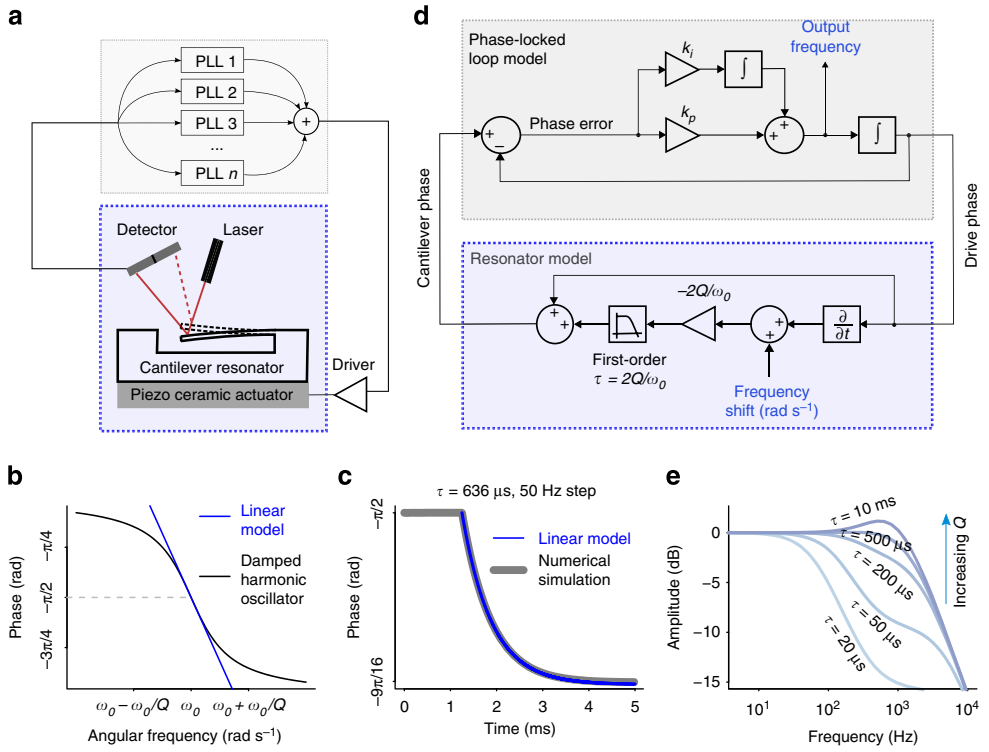


**Figure 1 | Open loop time constant, $\tau$ of a harmonic oscillator affects the closed-loop system dynamics.** (**a**) Schematic representation of the multimode resonator system operating in closed loop with multiple PLLs (one per resonant mode). (**b**) To make a linear model for the resonator phase response around its resonant frequency, we use the first-order Taylor series of the tangent function and find a slope of $-2Q/\omega_0$ (blue line). (**c**) Damped harmonic oscillator phase response to a step in the drive frequency, calculated by time-domain numerical integration (grey line), and a linearized model as a first-order lowpass filter (blue line; see Supplementary Note 1). (**d**) Linear phase-domain model of a resonator-PLL system. The resonator model shown in the blue-dotted box (bottom) is identical to a lowpass filter with a bandwidth of $1/\tau$ and a DC gain of zero dB, but depicted differently so that it can provide access to resonant frequency changes as an input (see Supplementary Note 2). Note that the resonator model has a positive feed-forward path that cancels with the PLL's negative feedback path and the PLL integrator cancels with the differentiator in the resonator model (Supplementary Fig. 2a). (**e**) Calculated frequency responses of resonator-PLL systems with varying resonator time constants, $\tau$, using the Laplace-domain phase model in **d**. It is evident that at higher frequencies, the resonator-PLL system response is substantially influenced by the resonator quality factor. The results are plotted for a single arbitrarily chosen $k_p$ and $k_i$ setting.

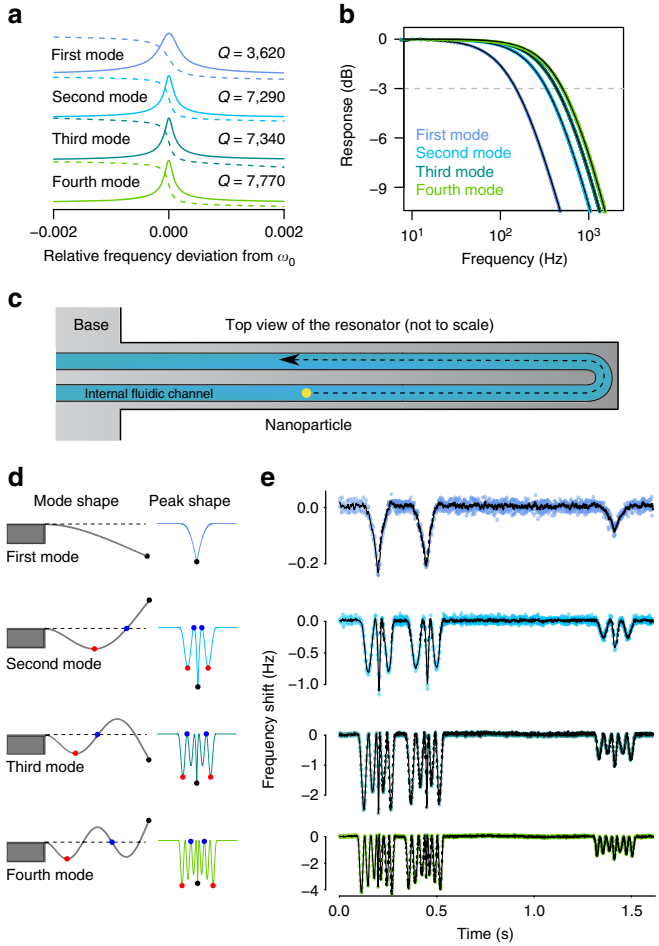


**Figure 2 | Weighing nanoparticles using multiple vibrational modes of an SNR.** After measuring resonant frequencies and quality factors of the first four modes, we set the PLL gains to obtain a flat frequency response with bandwidths between 150 and 500 Hz, and then measure frequency modulation signals generated by nanoparticles passing through the resonator oscillating in four bending modes, simultaneously. (**a**) Transfer function amplitude (solid lines) and phase (dashed lines) for each of the first four bending modes of the resonator measured by a lock-in amplifier. (**b**) Measured frequency responses of the resonator-PLL systems for the four resonant modes (coloured dots) with overlaid predicted first-order transfer functions (black lines). See Supplementary Note 4 for the transfer function measurement method. (**c**) Schematic diagram showing the layout of the internal channel of the resonator along with an example nanoparticle flow path. (**d**) Schematic diagram of the calculated bending profiles of the first four resonant modes (left) along with the corresponding frequency deviations (right) when a particle with constant velocity travels through the resonator similar to that shown in **c**. The locations of several nodes and antinodes are depicted both on the mode profiles and on the frequency modulation signals with matching colours. (**e**) Simultaneous frequency measurements of the first four bending modes as two 150-nm and one 100-nm gold nanoparticle transit through the resonator. Raw data are shown as dots. Because of the lower signal-to-noise ratio in the first and second modes, the overlaid black lines show the data filtered with a 5-point and a 3-point moving average filter, respectively. Black lines for third and fourth modes are unfiltered.

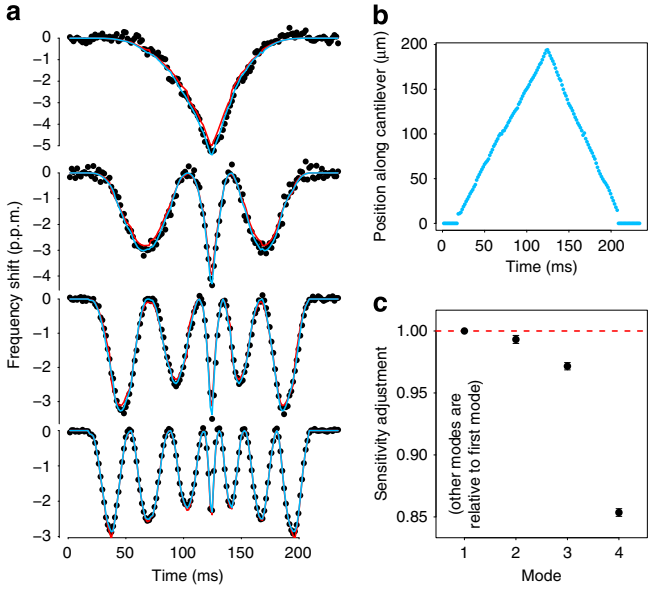


**Figure 3 | Multimode measurements yield the trajectory of a flowing nanoparticle.** (**a**) Four mode data for a single particle (black points) fit to the expected peak shape[22] when the particle has a fixed mass and can be at any position at any time (red lines), and when the mode sensitivities are allowed to vary as well (blue lines). Note the systematic deviations of the red fits at the local minima for each signal. (**b**) Position of the particle over time, estimated from the data in **a**. (**c**) Estimated sensitivities of other modes compared with the expected values. Points and error bars are the mean and s.e.m. of 31 150-nm gold particles, each of which were fit individually to a model, in which the mode sensitivities were allowed to vary relative to the expected values.

to simultaneously extract mass and position of nanoparticle pairs flowing through the resonator. As shown in Fig. 4a, a single mode provides limited information about the particles. However, by utilizing all four modes it was possible to resolve the position and mass of both particles as they flowed through the resonator (Fig. 4b). The first example shows two particles following each other in the channel (illustrated in Fig. 4c). We can see that at the tip of the resonator the heavier particle slows down because of higher centrifugal force opposite to the direction of the flow[12]. The second case shows two particles following each other very closely in the first half of the channel. When the particles turn at the tip of the resonator, one of them veers away from the initial flow path to a path where the flow velocity is slower.

**Noise analysis**. The precision of our position and mass estimates will depend on the noise properties of the modal measurements. To assess this, we simultaneously recorded 1-min noise waveforms from each mode and found that all the modes exhibited minimum Allan deviations at gate times between 20 and 500 ms, ideal for fast particle measurements (Fig. 5a, coloured circles). The measured minimum fractional Allan deviations range from 7 to 19 p.p.b., which are more than 3,000-fold lower than what would have been achievable for thermally driven (free-running) resonators (Fig. 5a, solid lines). However, if we could improve the dynamic range of our detector such that all modes could be oscillated at the onset of mechanical nonlinearity (measured here as 94, 91, 92 and 97 dB above the thermal fluctuations), we could improve the frequency stabilities by over an order of magnitude (Fig. 5a, dashed lines). Calculation details for Allan deviation and thermal noise limits are provided in Methods and in ref. 18.

As the nanoparticles are inside an opaque silicon beam, we cannot visually observe their location for comparison against our measurements. However, assuming a well-validated model of how point-mass loading affects modal frequencies[19,22], we can estimate the precision using the measured frequency noise.

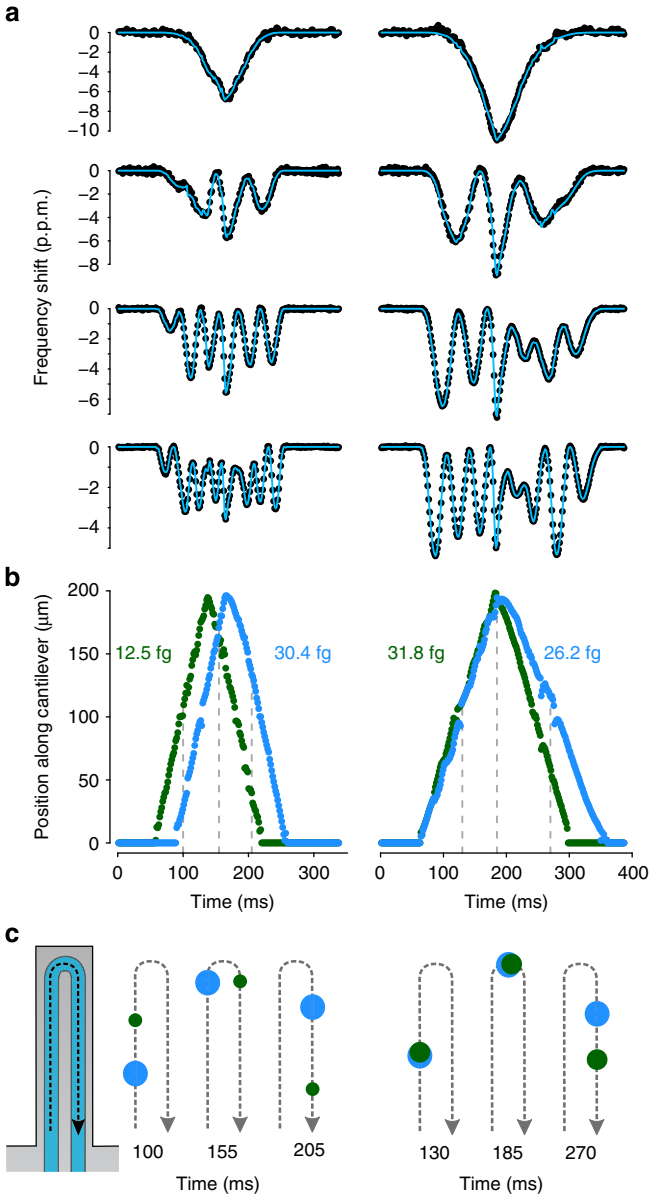


**Figure 4 | Fast multimode measurements resolve dynamic distribution of nanoparticle masses.** (**a**) Four mode data (black dots) from two instances in which two particles nearly simultaneously traversed the resonator, and a fit to a model in which two particles are simultaneously present (blue lines). (**b**) Calculated masses and positions of each particle during their transits in the resonator as a function of time. (**c**) Illustration showing particle locations at varying time points (noted as dashed lines in **b**) as they flow through the resonator (not to scale).

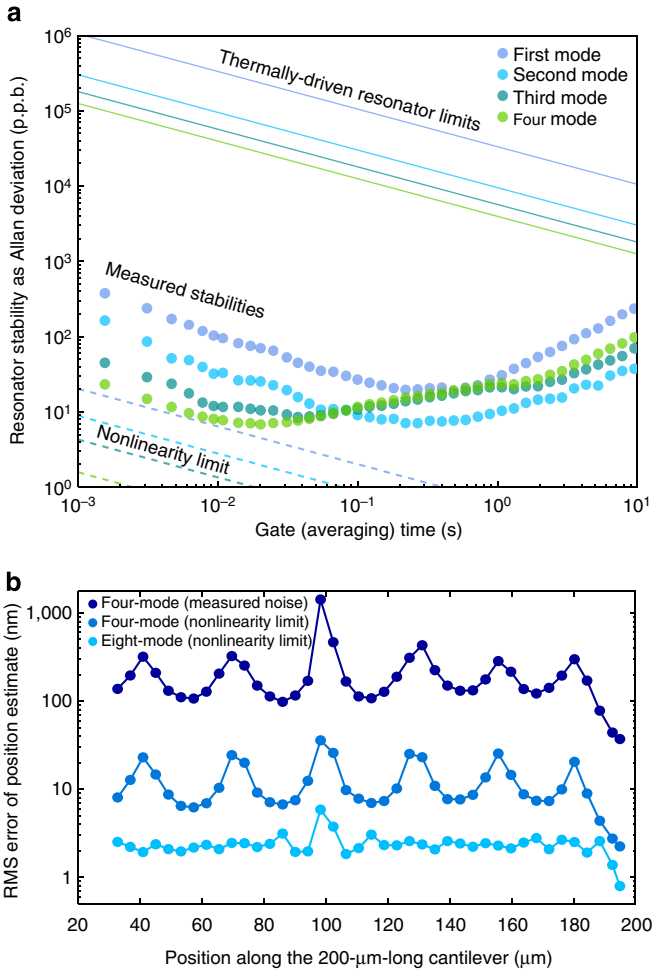


**Figure 5 | Multimode frequency stability limits mass position precision.** (**a**) Measured fractional Allan deviations of four modes of the resonator (coloured circles), while they are simultaneously oscillated, as a function of averaging times. For comparison, we also show the theoretical noise limits for this cantilever when thermally driven (solid lines) or individually driven to the onset of nonlinear behaviour (dashed lines). (**b**) Root-mean-square error of the position estimation of a 30-fg (~150-nm gold) particle as a function of its position along the resonator length. The error is calculated by running the fitting algorithm on simulated signals of identical particles passing through the resonator in 150 ms corrupted with experimentally measured noise (dark blue), thermal noise when maximally driven in the first four modes (blue) and thermal noise when maximally driven in the first eight modes (teal).

To determine the precision of the position estimation due to frequency noise alone, we fit a set of model-generated frequency signals corrupted with the recorded waveforms of frequency noise. We first generated the four-mode frequency modulation signals for a 150-nm gold nanoparticle (30 fg) making a 150-ms transit through the resonator. We then randomly sampled 250 short contiguous subsets from our noise measurements, added each to the theoretical particle waveforms and solved for the mass and positions to obtain their standard errors. This explicitly takes into account the frequency spectrum of our noise. In our case of four modes, we can determine the position of a 150-nm particle with a typical RMS error of 152 nm along the length of the resonator and 37 nm at the tip (Fig. 5b, black circles). While this position precision will improve with increasing particle mass, the uncertainty of the mass estimate (41 attograms) is independent of particle mass. In addition, while we simulate a 150-ms particle transit, we estimate a position for each time point, rendering the position precision effectively independent of the transit time.

Although previous work has questioned the value of extra higher-order modes[22], we compared our position precision using four modes against using only the first two or three modes and found a notable improvement with each extra mode introduced (Supplementary Fig. 6a). Similarly, achieving thermally limited noise while driving eight modes just below the onset of nonlinearity would improve the position precision by two orders of magnitude (Fig. 5b). Even greater gains could be achieved by using smaller resonators—a 10-fold shorter SNR similar to those in ref. 11 with similar stabilities in eight modes would enable analysing single virions or extracellular vesicles (~100 nm) with 4-nm position precision (see Supplementary Note 6 and Supplementary Fig. 6b). However, smaller resonators

come at the cost of high resonant frequencies, requiring specialized actuation and detection schemes. To operate smaller resonators, future systems may employ optimized piezoresistor sensors[39–41] and alternate optical[42–44] or electrical[45–47] low noise transduction schemes that can sustain multiple resonances at high frequencies[23].

## Discussion

The ability to resolve nanoparticle pairs in close proximity in a resonator suggests the possibility of observing bimodal mass distributions within a population of single particles, or resolving high-aspect-ratio shapes versus more spherical shapes in solution. In addition, to be able to monitor the dynamic changes in the mass distributions could be used for online monitoring of the assembly of engineered nanoparticles such as DNA origami or nanoparticles designed for nanomedicine. The ability of mechanical resonators to study the distribution of mass in analytes will ultimately depend on the resonator size, the number of modes measured and the frequency measurement precision. Improvements in any/all of these three areas, perhaps in parallel with mass tagging at specific locations, could ultimately enable analysing the structure of lighter biological particles such as phage, viruses or exosomes in solution, or single proteins with nanomechanical mass spectroscopy in vacuum, which are currently difficult to resolve with optical techniques and laborious to observe with other methods. The same approach, when applied to larger resonators that can sustain bacteria or mammalian cells, could ultimately be used to obtain high-throughput mass tomography of single living cells.

We believe that the presented method will also prove useful for large-scale integration of resonators. A carefully configured PLL array can oscillate an array of resonators individually with combined-detector and combined-actuator signals. The presented ability of engineering the system responses of individually addressable (by resonant frequency) resonators will be pivotal to such large-scale implementations. Such an approach could enable systems exploiting resonators ranging from very sensitive gas sensors to artificial nose applications to high-throughput cell analysers.

## Methods

**Device fabrication.** The SNR used in the experiments was fabricated using a microfabrication process[12,13] that was carried out at Innovative Micro Technologies, Santa Barbara, CA. The device includes a hollow microcantilever free to oscillate in a vacuum-sealed cavity with an on-chip getter, enabling long-term high-quality factor operation. The embedded fluidic channel in the SNR is accessed from the two sides by two larger (50 μm by 20 μm) bypass channels, which have two fluidic ports each. The top-side of the device is protected by a glass wafer, which enables optical access to the resonator.

**PLL implementation.** The PLL was implemented on an Altera Cyclone IV FPGA on a DE2–115 development board from Terasic Technologies. The board clock signal was generated by a 100-MHz oven-controlled crystal oscillator (Abracon AOCJY2). Analogue-to-digital and digital-to-analogue data conversion were performed using a daughter board from Terasic with two A/D converters and two D/A converters, all 14-bit and running at 100 MHz, connected to the FPGA via a high-speed mezzanine connector. The FPGA code was written in Verilog and compiled using Quartus II 12.1 (Altera). The code includes 12 identical PLL modules. Each module utilizes a multiplier and a low-pass filter as a phase error detector (Supplementary Fig. 2c). The low-pass filter is a second-order cascaded integrator-comb-decimating filter[48], with a variable rate change factor (and thus variable bandwidth). Unfortunately, this phase detector is sensitive to both the phase and the amplitude of the input:

$$\begin{aligned}\phi_{\text{detector}} &= \text{Lowpass}[x_{\text{in}}(t)\times x_{\text{NCO}}(t)]\\ &= \text{Lowpass}[A_{in}\sin(\omega t+\phi_{in})\sin(\omega t)]r\\ &= \text{Lowpass}\left[A_{in}\frac{\cos(\phi_{in})-\cos(2\omega t+\phi_{in})}{2}\right]\\ &= \frac{A_{in}}{2}\cos(\phi_{in})\end{aligned} \tag{2}$$

The phase detector is therefore linear around $\phi_{\text{in}}=-\pi/2$, where the PLL locks; however, it has a gain that depends on the input signal amplitude. Therefore, we calculate the input amplitude $A_{\text{in}}$ and divide the phase error by it. This is implemented by multiplying the input signal by both the sine and cosine outputs of the numerically controlled oscillator (NCO), low-pass-filtering both and calculating the sum of the squared values, yielding the input magnitude squared. We then use a look-up table to calculate an appropriate fractional gain to cancel out the input magnitude, as both square root and division operations are logic-intensive and slow, often not meeting timing requirements. This normalized error signal is then split into two paths, one of which is rescaled and integrated (with some finite frequency bounds outside which the integration saturates, so that the PLL cannot accidentally lock to other modes), and the other of which is rescaled and then summed with the integral path. This signal is then fed into a 35-bit NCO with a frequency resolution of 2.9 mHz.

Each PLL module is connected to a 32-bit CPU implemented on the FPGA (Nios II, Altera). The CPU can both write to control registers inside the PLL to set parameters such as the proportional or integral gains or the output drive amplitude, as well as read various PLL state variables such as the current NCO frequency. In our system, the DE2–115 board is connected to a computer via gigabit ethernet, and C code running on the Nios II processor creates a simple server through which the PC can connect and read/write PLL registers. Writing to registers occurs over a TCP connection to ensure reliability; however, the NCO frequency is transmitted from the FPGA via UDP multicast, allowing for much lower overhead and higher bandwidth. We find that we can easily transmit uncompressed frequency data (32-bit integers) at a rate of over 100 kHz with no dropped packets. On the PC, we have implemented a LabView (National Instruments) software to save this data stream, as well as let us easily set the PLL control register values over the TCP connection.

In the current configuration, each PLL module takes up roughly 6,500 logic cells (out of 114,480), 11 $18\times18$-bit multipliers (out of 266 total), and four M9K memory blocks (out of 432 total) of an Altera Cyclone IV FPGA on a DE2–115 development board. As the CPU takes up roughly 15,000 logic cells, two $18\times18$-bit multipliers, and 253 M9K memory blocks, logic cells are the limiting factor in increasing the number of parallel PLLs running on a single FPGA. In the current implementation, we can fit 14–15 PLLs on our FPGA though future implementations with higher-end FPGAs could fit many more—for example, the Altera Stratix III EP3SL340 could likely fit around 50 PLLs.

**Single-particle fits.** We rely on the following equation given in ref. 22 relating the relative frequency shift $(\frac{\omega_{\Delta m,n}}{\omega_n})$ of a resonator of mass $m_0$ operating in mode $n$, when loaded with a point mass $\Delta m$ at a position $z$:

$$\frac{\omega_{\Delta m,n}}{\omega_n}=\frac{1}{\sqrt{1+\frac{\Delta m}{m_0}U_n^2(z)}} \tag{3}$$

where $U(z)$ is given by

$$U(z)=\cos(\kappa_n z)-\cosh(\kappa_n z)+c_n(\sin(\kappa_n z)-\sinh(\kappa_n z)) \tag{4}$$

with $\kappa_n$ being the $n$th root of $\cos(x)\cosh(x)=-1$ and $c_n=(\sin(\kappa_n)-\sinh(\kappa_n))/(\cos(\kappa_n)+\cosh(\kappa_n))$. In this case, $z$ is parameterized such that 0 represents the base of the cantilever and 1 is the tip of the cantilever.

To account for the reduced sensitivity in higher modes (as compared with what is expected in (2)), we modify this model slightly by including a sensitivity adjustment parameter $s_n$, which is fit for all modes except the first ($s_1$ is defined as 1).

$$\frac{\omega_{\Delta m,n}}{\omega_n}=\frac{s_n}{\sqrt{1+\frac{\Delta m}{m_0}U_n^2(z)}} \tag{5}$$

To fit particle trajectories, we follow ref. 22 by attempting to minimize the residual squared error $\chi^2$ of the normalized signals (fit errors are divided by the s.d. of the signal, such that a unit residual error is equally penalized for all modes). Free parameters in this fit are noted in red:

$$\chi^2(z,\Delta m/m_0,s)=\sum_{t=0}^{T}\sum_{n=1}^{N}\frac{1}{\sigma_n^2}\left(\frac{\omega_{\Delta m,n}}{\omega_n}-\frac{s_n}{\sqrt{1+\frac{\Delta m}{m_0}U_n^2(z_t)}}\right)^2 \tag{6}$$

Here $z$ is a vector consisting of one value per time point $t$, and is not constrained based on expected flow path. $T$ is the number of timepoints, $t$ indexes the timepoints, $N$ is the number of modes, $n$ indexes the modes and $\sigma_n$ is the RMS noise in mode $n$.

**Two-particle fits.** We proceed in a very similar manner for the two-particle fits, minimizing the following objective function[19]:

$$\chi^2(z,\Delta m/m_0,s)=\sum_{t}\sum_{n=1}^{N}\frac{1}{\sigma_n^2}\left(\frac{\omega_{\Delta m,n}}{\omega_n}-\frac{s_n}{\sqrt{1+\frac{\Delta m_1}{m_0}U_n^2(z_{1,t})+\frac{\Delta m_2}{m_0}U_n^2(z_{2,t})}}\right)^2 \tag{7}$$

**Noise analysis calculations.** The fractional Allan deviation, $\sigma_A(\tau_A)$, of the frequency of an oscillator in a time period of $\tau_A$ is defined as in ref. 49:

$$\sigma_A(\tau_A) = \sqrt{\sigma_A^2(\tau_A)} \approx \sqrt{\frac{1}{2(N-1)}\sum_{k=2}^{N}\left(\frac{\bar{f}_k - \bar{f}_{k-1}}{f_0}\right)^2} \quad (8)$$

where $\bar{f}_k$ is the time average of the frequency measurement in the $k^{\text{th}}$ time interval of length $\tau_A$ within a total of $N$ intervals, and $f_0$ is the mean oscillation frequency calculated over the entire duration of the noise measurement. The fractional Allan deviation of a resonator due to thermal noise is given as[18]:

$$\sigma_A^{th}(\tau_A) = \sqrt{\frac{\langle x_{\text{thermal}}^2\rangle}{\langle x_{\text{driven}}^2\rangle}\frac{1}{\omega_0 Q \tau_A}} \quad (9)$$

where $\langle x_{\text{thermal}}^2\rangle$ is the mean squared displacement because of thermal vibration, and $\langle x_{\text{driven}}^2\rangle$ is the mean squared displacement when driven. For a purely thermally driven cantilever, the ratio of these quantities is one.

## References


1. Moser, J., Eichler, A., Güttinger, J., Dykman, M. I. & Bachtold, A. Nanotube mechanical resonators with quality factors of up to 5 million. *Nat. Nanotechnol.* **9,** 1007–1011 (2014).
2. Moser, J. *et al.* Ultrasensitive force detection with a nanotube mechanical resonator. *Nat. Nanotechnol.* **8,** 493–496 (2013).
3. Husale, S., Persson, H. H. J. & Sahin., O. DNA nanomechanics allows direct digital detection of complementary DNA and microRNA targets. *Nature* **462,** 1075–1078 (2009).
4. Dong, M. & Sahin., O. A nanomechanical interface to rapid single-molecule interactions. *Nat. Commun.* **2,** 247 (2011).
5. Rugar, D., Budakian, R., Mamin, H. J. & Chui, B. W. Single spin detection by magnetic resonance force microscopy. *Nature* **430,** 329–332 (2004).
6. Zolfagharkhani, G. *et al.* Nanomechanical detection of itinerant electron spin flip. *Nat. Nanotechnol.* **3,** 720–723 (2008).
7. Zhang, X. C., Myers, E. B., Sader, J. E. & Roukes., M. L. Nanomechanical torsional resonators for frequency-shift infrared thermal sensing. *Nano Lett.* **13,** 1528–1534 (2013).
8. Jensen, K., Kim, K. & Zettl., A. An atomic-resolution nanomechanical mass sensor. *Nat. Nanotechnol.* **3,** 533–537 (2008).
9. Chaste, J. *et al.* A nanomechanical mass sensor with yoctogram resolution. *Nat. Nanotechnol.* **7,** 301–304 (2012).
10. Hanay, M. S. *et al.* Single-protein nanomechanical mass spectrometry in real time. *Nat. Nanotechnol.* **7,** 602–608 (2012).
11. Olcum, S. *et al.* Weighing nanoparticles in solution at the attogram scale. *Proc. Natl Acad. Sci. USA* **111,** 1310–1315 (2014).
12. Lee, J., Shen, W., Payer, K., Burg, T. P. & Manalis., S. R. Toward attogram mass measurements in solution with suspended nanochannel resonators. *Nano Lett.* **10,** 2537–2542 (2010).
13. Burg, T. P. *et al.* Weighing of biomolecules, single cells and single nanoparticles in fluid. *Nature* **446,** 1066–1069 (2007).
14. Godin, M. *et al.* Using buoyant mass to measure the growth of single cells. *Nat. Methods* **7,** 387–390 (2010).
15. Park, K. *et al.* Measurement of adherent cell mass and growth. *Proc. Natl Acad. Sci. USA* **107,** 20691–20696 (2010).
16. Grover, W. H. *et al.* Measuring single-cell density. *Proc. Natl Acad. Sci. USA* **108,** 10992–10996 (2011).
17. Bargatin, I. *et al.* Large-scale integration of nanoelectromechanical systems for gas sensing applications. *Nano Lett.* **12,** 1269–1274 (2012).
18. Gavartin, E., Verlot, P. & Kippenberg, T. J. Stabilization of a linear nanomechanical oscillator to its thermodynamic limit. *Nat. Commun.* **4,** 2860 (2013).
19. Dohn, S., Schmid, S., Amiot, F. & Boisen, A. Position and mass determination of multiple particles using cantilever based mass sensors. *Appl. Phys. Lett.* **97,** 044103 (2010).
20. Hanay, M. S. *et al.* Inertial imaging with nanomechanical systems. *Nat. Nanotechnol.* **10,** 339–344 (2015).
21. Albrecht, T. R., Grütter, P., Horne, D. & Rugar, D. Frequency modulation detection using high-Q cantilevers for enhanced force microscope sensitivity. *J. Appl. Phys.* **69,** 668 (1991).
22. Dohn, S., Svendsen, W., Boisen, A. & Hansen., O. Mass and position determination of attached particles on cantilever based mass sensors. *Rev. Sci. Instrum.* **78,** 103303 (2007).
23. Bargatin, I., Kozinsky, I. & Roukes, M. L. Efficient electrothermal actuation of multiple modes of high-frequency nanoelectromechanical resonators. *Appl. Phys. Lett.* **90,** 093116 (2007).
24. Gil-Santos, E. *et al.* Nanomechanical mass sensing and stiffness spectrometry based on two-dimensional vibrations of resonant nanowires. *Nat. Nanotechnol.* **5,** 641–645 (2010).
25. Wang, Z., Lee, J. & Feng, P. X.-L. Spatial mapping of multimode Brownian motions in high-frequency silicon carbide microdisk resonators. *Nat. Commun.* **5** (2014).
26. Mahboob, I., Mounaix, M., Nishiguchi, K., Fujiwara, A. & Yamaguchi., H. A multimode electromechanical parametric resonator array. *Sci. Rep.* **4,** 4448 (2014).
27. Greywall, D., Yurke, B., Busch, P., Pargellis, A. & Willett, R. Evading amplifier noise in nonlinear oscillators. *Phys. Rev. Lett.* **72,** 2992–2995 (1994).
28. Feng, X. L., White, C. J., Hajimiri, A. & Roukes., M. L. A self-sustaining ultrahigh-frequency nanoelectromechanical oscillator. *Nat. Nanotechnol.* **3,** 342–346 (2008).
29. Durig, U., Steinauer, H. R. & Blanc, N. Dynamic force microscopy by means of the phase-controlled oscillator method. *J. Appl. Phys.* **82,** 3641–3651 (1997).
30. Kouh, T., Basarir, O. & Ekinci, K. L. Room-temperature operation of a nanoelectromechanical resonator embedded in a phase-locked loop. *Appl. Phys. Lett.* **87,** 113112 (2005).
31. Nony, L. *et al.* Noncontact atomic force microscopy simulator with phase-locked-loop controlled frequency detection and excitation. *Phys. Rev. B* **74,** 235439 (2006).
32. Fukuma, T., Yoshioka, S. & Asakawa, H. Wideband phase-locked loop circuit with real-time phase correction for frequency modulation atomic force microscopy. *Rev. Sci. Instrum.* **82,** 073707 (2011).
33. Bouloc, J. *et al.* in *2012 IEEE Sensors* 1–4 (Taipei, 2012).
34. Ihn, T. *Electronic Quantum Transport in Mesoscopic Semiconductor Structures* (Springer, 2004).
35. Degen, C. L., Meier, U., Lin, Q., Hunkeler, A. & Meier, B. H. Digital feedback controller for force microscope cantilevers. *Rev. Sci. Instrum.* **77,** 043707–043708 (2006).
36. Kilpatrick, J. I., Gannepalli, A., Cleveland, J. P. & Jarvis, S. P. Frequency modulation atomic force microscopy in ambient environments utilizing robust feedback tuning. *Rev. Sci. Instrum.* **80,** 023701 (2009).
37. Bouloc, J. *et al.* FPGA-based programmable digital PLL with very high frequency resolution. in *18th IEEE International Conference on Electronics, Circuits and Systems (ICECS)* 370–373 (Beirut, Lebanon, 2011).
38. Gardner, F. M. *Phaselock Techniques* 3rd edn (John Wiley and Sons, 2005).
39. Park, S.-J., Doll, J. C., Rastegar, A. J. & Pruitt., B. L. Piezoresistive cantilever performance-part ii: optimization. *J. Microelectromech. Syst.* **19,** 149–161 (2010).
40. Park, S.-J., Doll, J. C. & Pruitt., B. L. Piezoresistive Cantilever performance-part i: analytical model for sensitivity. *J. Microelectromech. Syst.* **19,** 137–148 (2010).
41. Sansa, M., Fernández-Regúlez, M., Llobet, J., San Paulo, Ã. & Pérez -Murano, F. High-sensitivity linear piezoresistive transduction for nanomechanical beam resonators. *Nat. Commun.* **5,** 4313 (2014).
42. Li, M., Pernice, W. H. P. & Tang, H. X. Broadband all-photonic transduction of nanocantilevers. *Nat. Nanotechnol.* **4,** 377–382 (2009).
43. Sampathkumar, A., Ekinci, K. L. & Murray, T. W. Multiplexed optical operation of distributed nanoelectromechanical systems arrays. *Nano Lett.* **11,** 1014–1019 (2011).
44. Basarir, O., Bramhavar, S. & Ekinci., K. L. Motion transduction in nanoelectromechanical systems (NEMS) arrays using near-field optomechanical coupling. *Nano Lett.* **12,** 534–539 (2012).
45. Truitt, P. A., Hertzberg, J. B., Huang, C. C., Ekinci, K. L. & Schwab, K. C. Efficient and sensitive capacitive readout of nanomechanical resonator arrays. *Nano Lett.* **7,** 120–126 (2007).
46. Unterreithmeier, Q. P., Weig, E. M. & Kotthaus, J. P. Universal transduction scheme for nanomechanical systems based on dielectric forces. *Nature* **458,** 1001–1004 (2009).
47. Faust, T., Krenn, P., Manus, S., Kotthaus, J. P. & Weig, E. M. Microwave cavity-enhanced transduction for plug and play nanomechanics at room temperature. *Nat. Commun.* **3,** 728 (2012).
48. Hogenauer., E. An economical class of digital filters for decimation and interpolation. *IEEE Trans. Acoustics Speech Signal Process.* **29,** 155–162 (1981).
49. Barnes, J. A. *et al.* Characterization of Frequency Stability. *IEEE Trans. Instrum. Measure.* **IM-20,** 105–120 (1971).
50. Kobayashi, K., Yamada, H. & Matsushige, K. Frequency noise in frequency modulation atomic force microscopy. *Rev. Sci. Instrum.* **80,** 043708 (2009).


## Acknowledgements

We thank John Sader and Michael Roukes for productive discussions about this work. This work was supported by Institute for Collaborative Biotechnologies through grant W911NF-09-0001 from the US Army Research Office. The content of the information does not necessarily reflect the position or the policy of the Government, and no official endorsement should be inferred. This work was additionally supported by Center for Integration of Medicine and Innovative Technology Contract 09–440 and National

Science Foundation Grant 1129359. N.C. acknowledges support through NSF (award no. 1129359) and an MIT Poitras Fellowship.

## Author contributions

All authors contributed to the design of the study and writing of the manuscript. S.O. and N.C. performed the experiments and analysed the data.

## Additional information

**Supplementary Information** accompanies this paper at http://www.nature.com/naturecommunications

**Competing financial interests:** S.R.M. declares competing financial interests as a cofounder of Affinity Biosensors, which develops techniques relevant to the research presented. The remaining authors declare no competing financial interests.

**Reprints and permission** information is available online at http://npg.nature.com/reprintsandpermissions/

**How to cite this article:** Olcum, S. *et al.* High-speed multiple-mode mass-sensing resolves dynamic nanoscale mass distributions. *Nat. Commun.* 6:7070 doi: 10.1038/ncomms8070 (2015).

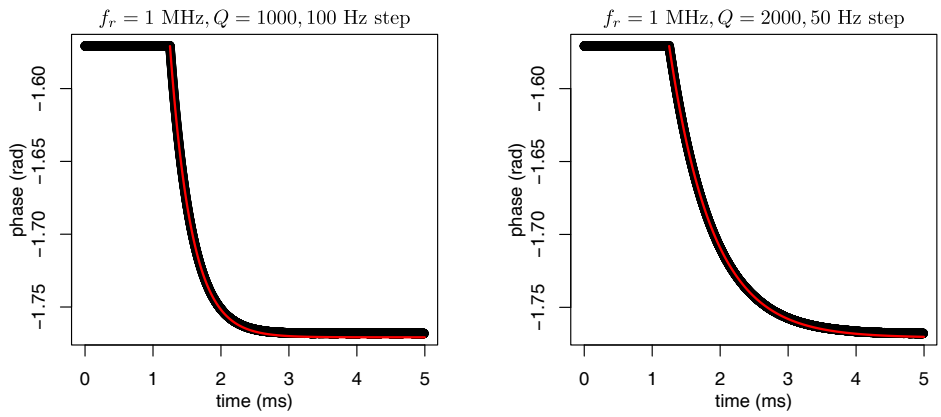


**Supplementary Figure 1: Resonator phase response to a step change in the drive frequency.** Time-domain simulation (forward Euler) of the phase response of a resonator to a step in the drive frequency (black), overlaid with the linear model prediction from equation (S8) in red.

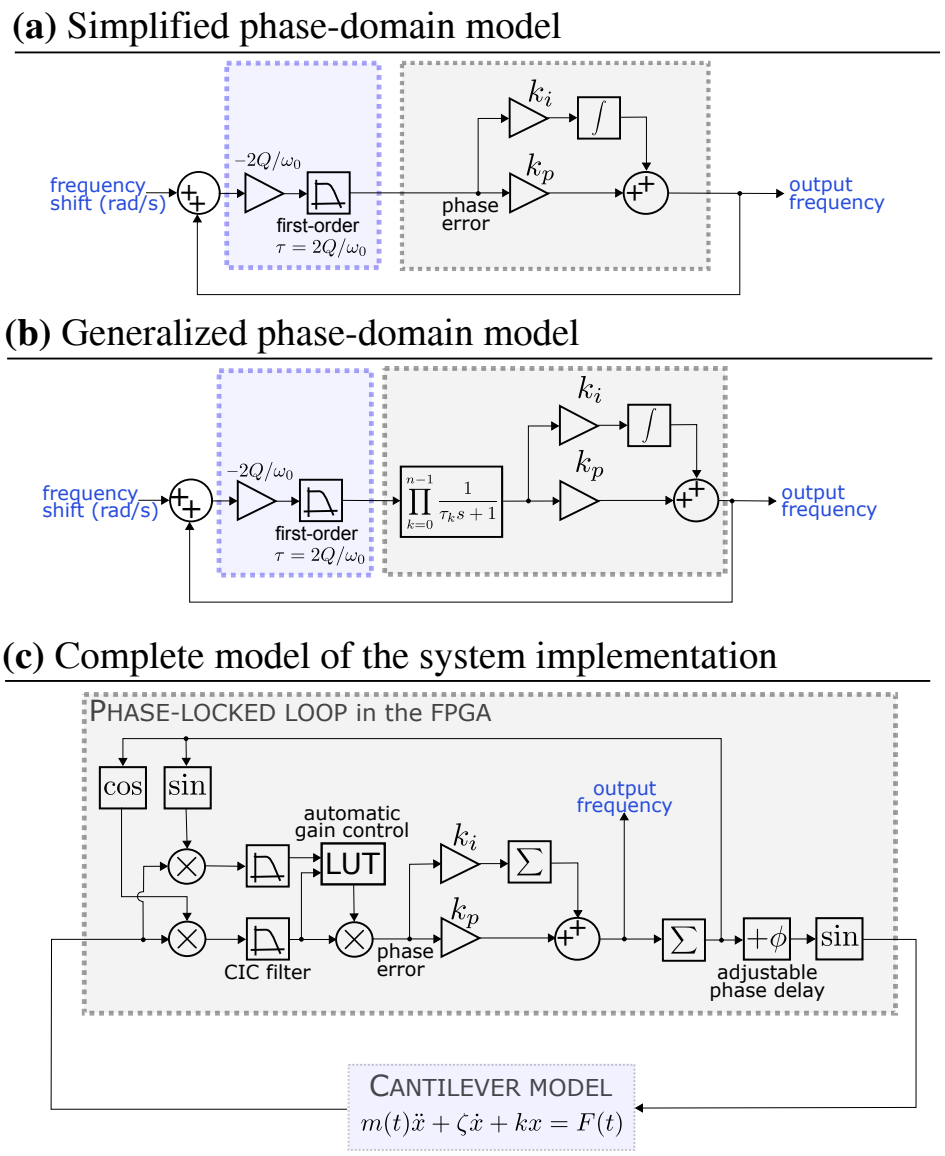


**Supplementary Figure 2: Block diagram representations of the models used to analyze a resonator-PLL loop.** **(a)** Phase-domain block diagram of simplified resonator-PLL closed loop system. The integrator representing the VCO in Figure 1d is cancelled by the differentiator of the resonator. **(b)** Phase-domain block diagram of the same system in (a) with $n-1$ poles inserted in the forward path. The additional poles increase the order of the characteristic polynomial of the closed loop transfer function for achieving $n^{th}$ order Butterworth filter response. **(c)** Complete block diagram representation of one element of the digital PLL array implemented on the FPGA.

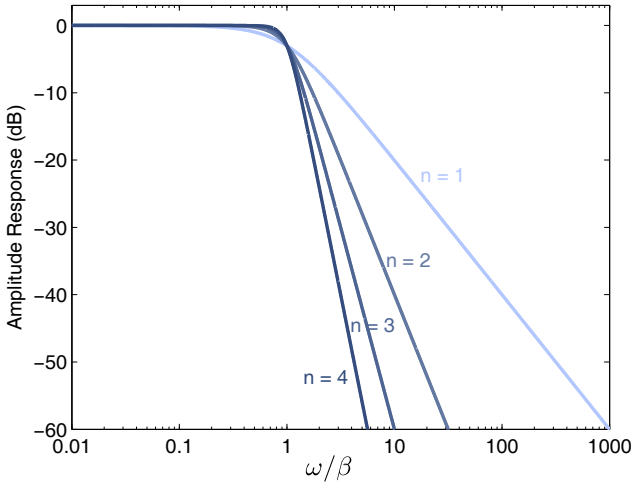


**Supplementary Figure 3: PLL parameters can be set to tailor closed loop dynamics.** Amplitude response of the closed loop system as a function of frequency normalized to desired bandwidth, $\beta$ when loop parameters given in Supplementary Table 1 are evaluated in (S13). The calculated responses are identical to that of a Butterworth low-pass filter of given order.

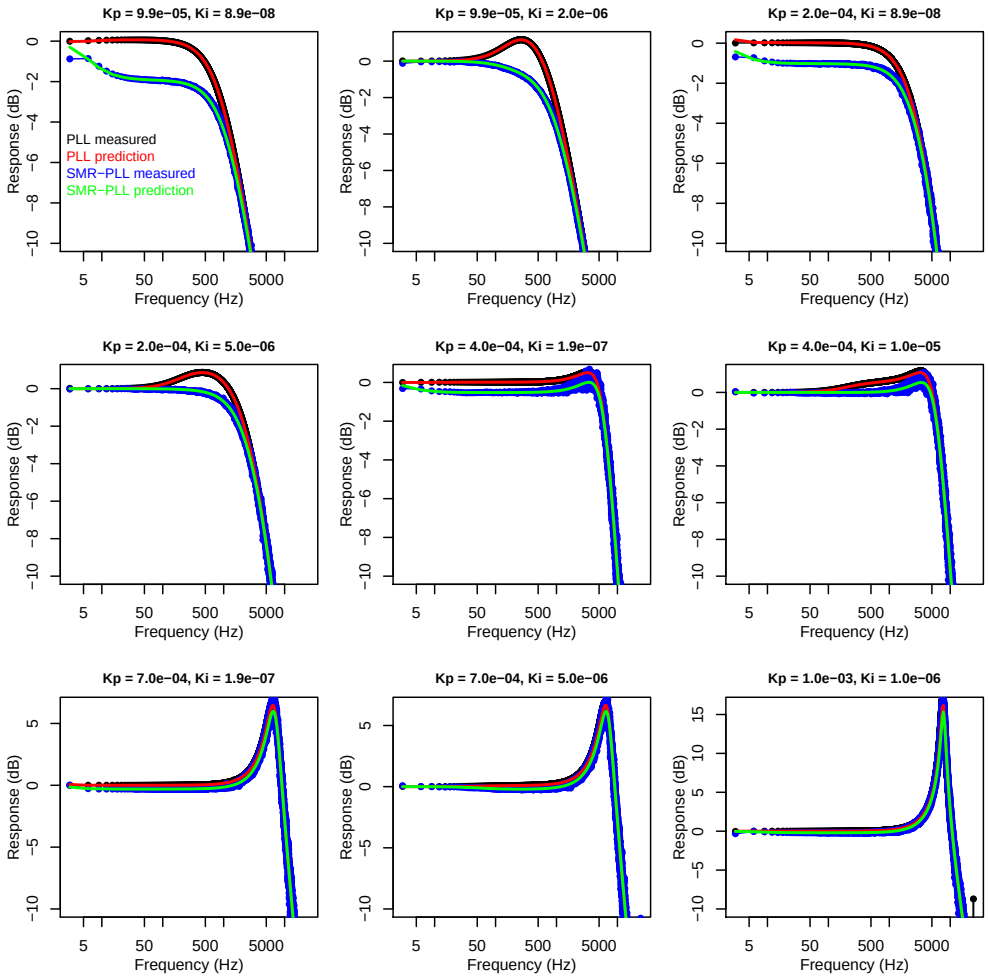


**Supplementary Figure 4: Comparison of measured versus modeled SMR and SMR-PLL transfer functions across varying PLL settings.** Calculated versus measured transfer functions for PLL alone (red and black) and SMR-PLL system (green and blue). The resonator was a 160 $\mu$m-long cantilever with a 3 $\times$ 5 $\mu$m embedded channel and a Q factor of approximately 2800. For the above plots, the CIC filter had rate change factor $R = 2048$.

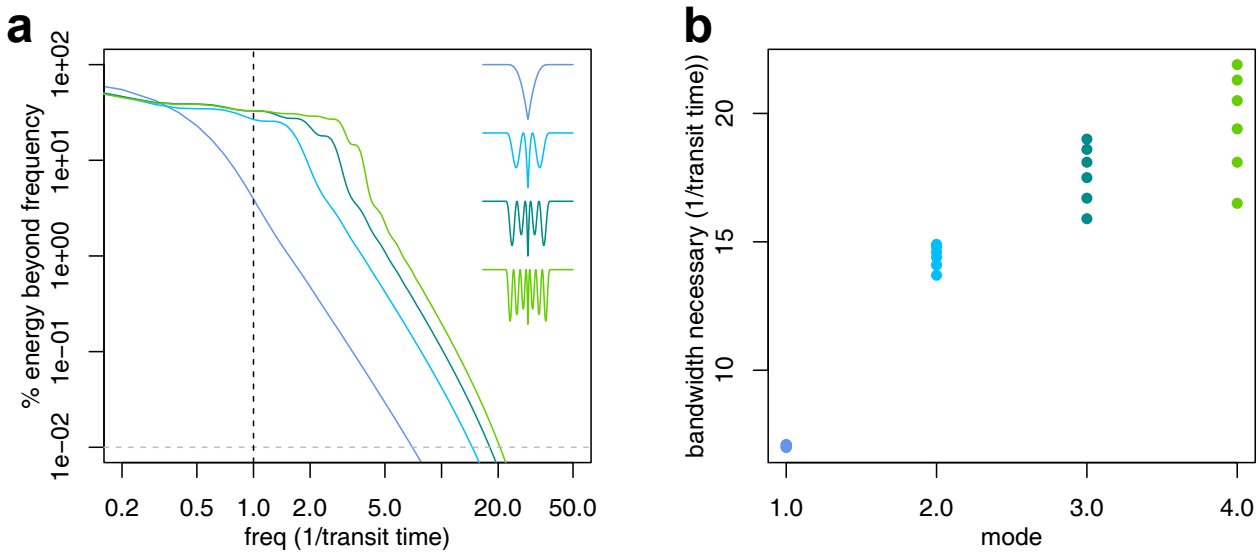


**Supplementary Figure 5: Spectral content of a particle's (demodulated) signal by mode.** **(a)** One minus integral of the energy spectral density, or what fraction of the signal energy is being lost if we exclude all energy at higher frequencies. Different colors represent increasing modes, for which the peak shapes are shown inset. **(b)** Required measurement bandwidth for recovering >99.99% of the energy, as a function of mode. Signal bandwidth depends on particle path - different dots for a single mode represent particles transiting 95%, 96%, 97%, 98%, 99% or 100% of the length of the cantilever. Cantilever resonant frequency signal shapes are calculated based on reference [1].

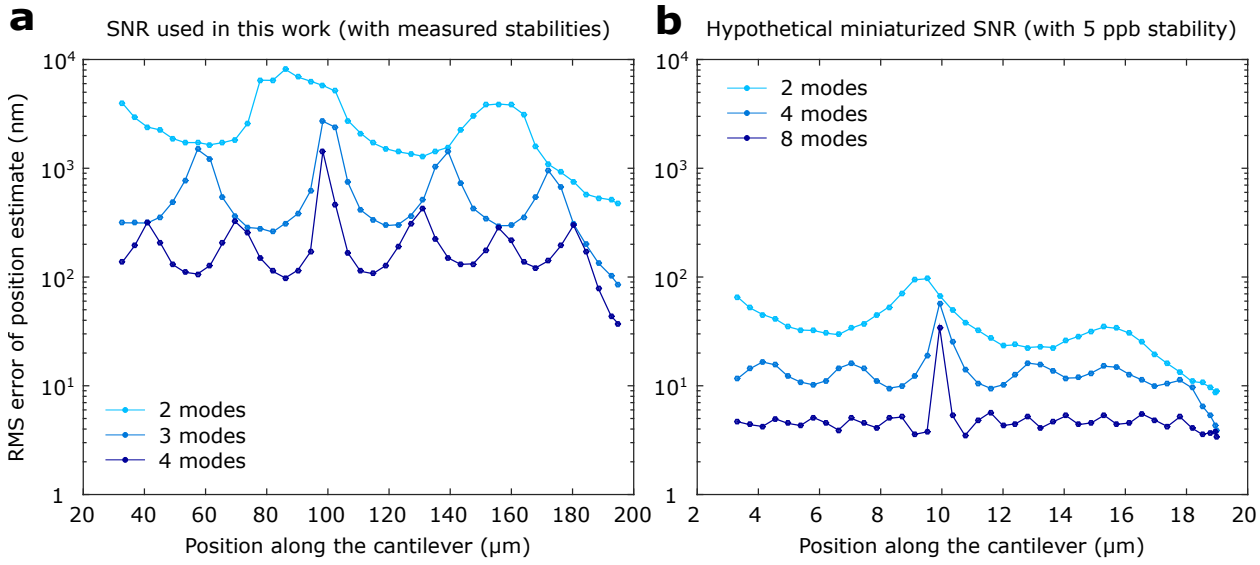


**Supplementary Figure 6: Miniaturization and/or additional modes and improve position precision,** i.e. RMS error of the position estimation. **(a)** The position precision of the SNR used in this work when the first two, three and four modes are used to weigh a 30-femtogram gold nanoparticle (150 nm). The curve for four modes on this plot is identical to the 4-mode curve in Figure 5. **(b)** The position precision of a hypothetical miniaturized SNR weighing a 80-attogram human immunodeficiency virus (∼100 nm) when first two, four and eight modes are oscillated with a frequency stability of 5 ppb.

**Supplementary Table 1: Resonator-PLL Loop parameters** for achieving $n^{th}$ order Butterworth filter response.

| $n$ | $k_p$ | $k_i$ | $\tau_1$ | $\tau_2$ | Additional Poles |
|---|---|---|---|---|---|
| 1 | $\beta$ | $k_p/\tau$ | | | 0 |
| 2 | $\beta/\sqrt{2}$ | $k_p/\tau$ | $\sqrt{2}/2\beta$ | | 1 |
| 3 | $\beta/2$ | $k_p/\tau$ | $(1 \pm j)/2\beta$ | $(1 \mp j)/2\beta$ | 2 |

## Supplementary Note 1 Phase-domain transfer function

As noted in the main text, for deriving the transfer function of the phase of a resonator, we analyze its time-domain response to an abrupt change in the excitation frequency. Prior to the frequency change, we assume that the resonator is oscillating in steady state with amplitude $A(\omega_0)$ and phase-delay $\theta(\omega_0)$ as given in references [2, 3],

$$A(\omega) = \frac{F_0/m}{\sqrt{(\omega_0^2 - \omega^2)^2 + (\omega_0\omega/Q)^2}} \tag{S1}$$

$$\theta(\omega) = \arctan\left(\frac{\omega_0\omega}{Q(\omega^2 - \omega_0^2)}\right) \tag{S2}$$

where $F_0$ is the amplitude of the driving force, $m$ is the effective mass of the resonator, $\omega_0$ is the resonant frequency and $Q$ is the quality factor of the resonator. When the excitation instantaneously changes its frequency, the resonator response is described by the sum of the zero-input response and the zero-state response as follows:

$$x(t) = A(\omega_0)e^{-t/\tau}\sin(\omega_0 t + \theta(\omega_0)) + A(\omega_1)(1 - e^{-t/\tau})\sin(\omega_1 t + \theta(\omega_1)) \tag{S3}$$

where $\omega_1$ is the new excitation frequency and $\tau = 2Q/w_0$. If we write (S3) in the form of $x(t) = A(t)\sin(\omega_1 t + \phi(t))$, $\phi(t)$ gives the phase of the resonator as a function of time. Therefore, we will use the following identity

$$a\sin(\psi_1) + b\sin(\psi_2) = c\sin\left(\psi_1 + \arctan\left[\frac{b\sin(\psi_2 - \psi_1)}{a + b\cos(\psi_2 - \psi_1)}\right]\right) \tag{S4}$$

We will entirely ignore the amplitude term $c$, other than noting that it is a time-dependent function. We'll use the following definitions to coerce (S3) into the form of (S4):

$$\begin{aligned} a &= A(\omega_1)(1 - e^{-t/\tau}) \\ b &= A(\omega_0)e^{-t/\tau} \\ \psi_1 &= \omega_1 t + \theta(\omega_1) \\ \psi_2 &= \omega_0 t + \theta(\omega_0) \\ \alpha &= \psi_2 - \psi_1 = (\omega_0 - \omega_1)t + \theta(\omega_0) - \theta(\omega_1) \end{aligned} \tag{S5}$$

Therefore we are left with:

$$x(t) = c(t)\sin\left(\omega_1 t + \theta(\omega_1) + \arctan\left[\frac{A(\omega_0)e^{-t/\tau}\sin(\alpha)}{A(\omega_1)(1 - e^{-t/\tau}) + A(\omega_0)e^{-t/\tau}\cos(\alpha)}\right]\right) \tag{S6}$$

Multiplying the *arctan* argument by $e^{t/\tau}/e^{t/\tau}$ and dividing by $A(\omega_0)/A(\omega_0)$, we get:

$$x(t) = c(t)\sin\left(\omega_1 t + \theta(\omega_1) + \arctan\left[\frac{\sin(\alpha)}{\frac{A(\omega_1)}{A(\omega_0)}(e^{t/\tau} - 1) + \cos(\alpha)}\right]\right)$$

Define $\tilde{\alpha} \equiv \theta(\omega_0) - \theta(\omega_1)$, and note that $\frac{A(\omega_1)}{A(\omega_0)} = \frac{\omega_0}{\omega_1}\cos(\tilde{\alpha}) \approx \cos(\tilde{\alpha})$, where the approximation is valid for very small frequency deviations.

$$x(t) = c(t)\sin\left(\omega_1 t + \theta(\omega_1) + \arctan\left[\frac{\sin(\alpha)}{\cos(\tilde{\alpha})e^{t/\tau} - \cos(\tilde{\alpha}) + \cos(\alpha)}\right]\right)$$

If the the frequency step $\omega_0 - \omega_1$ is very small, then $(\omega_0 - \omega_1)t$ is a very slow term compared to $e^{t/\tau}$, and we can approximate the time-varying $\alpha$ as the constant $\tilde{\alpha}$. Then the equation reduces to:

$$x(t) = c(t)\sin\left(\omega_1 t + \theta(\omega_1) + \arctan\left[\tan(\tilde{\alpha})e^{-t/\tau}\right]\right)$$

The Taylor expansion of $\arctan(\tan(\alpha)x) = x\tan(\tilde{\alpha}) - \frac{1}{3}\tan^3(\tilde{\alpha})x^3 + O(x^5)$. Noting that $\tilde{\alpha}$ is typically small justifies dropping all but the linear term, yielding

$$x(t) = c(t)\sin\left(\omega_1 t + \theta(\omega_1) + \tan(\tilde{\alpha})e^{-t/\tau}\right)$$

Approximating $\tan(x)$ with $x$

$$\begin{aligned} x(t) &= c(t)\sin\left(\omega_1 t + \theta(\omega_1) + (\theta(\omega_0) - \theta(\omega_1))e^{-t/\tau}\right) \\ &= c(t)\sin\left(\omega_1 t + \theta(\omega_0) + (\theta(\omega_1) - \theta(\omega_0))(1 - e^{-t/\tau})\right) \end{aligned} \tag{S7}$$

Noting that $\theta(\omega)$ is also a *tan* function, we approximate that with its $1^{st}$-order Taylor series around the resonant frequency, $\theta(\omega) = \theta(\omega_0) - \tau(\omega - \omega_0)$:

$$x(t) = c(t)\sin\left(\omega_1 t + \theta(\omega_0) - \tau(\omega_1 - \omega_0)(1 - e^{-t/\tau})\right) \tag{S8}$$

To verify that our approximations were reasonable, we compared our model predictions to time-domain simulations of a driven damped harmonic oscillator that experiences a step in the drive frequency. In our simulation, we estimate the phase delay based on the timing of zero-crossings (strictly, only zero-crossings where the signal is increasing). Defining the vector of resonator zero-crossing times as $t_{r0}$ and the vector of drive zero-crossing times as $t_{d0}$, we calculate the phase at every resonator zero-crossing as $\phi = \frac{t_{r0}[n] - t_{d0}[n]}{t_{d0}[n] - t_{d0}[n-1]}$. The results of this simulation, plotted as the black curves in Supplementary Figure 1, agree very well with the approximation in equation (S8) plotted as the red curves.

For calculating the phase domain transfer function of a resonator, we used the approximate expression in (S8), where the response of the resonator phase, $\phi(t)$, to a phase step of $-\tau(\omega_1 - \omega_0)$ at $t = 0$ is given as:

$$\phi(t) = \theta(\omega_0) - \tau(\omega_1 - \omega_0)(1 - e^{-t/\tau}) \tag{S9}$$

Note that $\theta(\omega_0)$ is the initial condition of the phase at $t = 0$. After normalizing the time-varying response in (S9) with the phase-step amplitude, we took its derivative to calculate the impulse response in time domain. Finally, the phase domain transfer function of a resonator to changes in its driving frequency is calculated by taking the Laplace-transform of the impulse response as:

$$\Phi(s) = \mathcal{L}\left(\frac{1}{\tau}e^{-t/\tau}\right) = \frac{1}{\tau s + 1} \tag{S10}$$

## Supplementary Note 2 Closed loop system function

We first model the resonator-PLL systems in phase domain using a commonly practiced $2^{nd}$-order Type-2 PLL [4] and the resonator response in (S10). We implement a model such that we can access the resonant frequency of the resonator as an input as well, by making the following modification:

$$\Phi(s) = \frac{1}{\tau s + 1} = 1 - \frac{\tau s}{\tau s + 1} \tag{S11}$$

which can be represented as shown in the blue box of Figure 1d. This model can then be further simplified by noting that the resonator has a positive feed-forward path that cancels with the PLL's negative feedback path. Furthermore, the PLL integrator cancels with the resonator differentiator. This allowed us to derive a simple, computationally tractable model (Supplementary Figure 2a) for the entire system. We derived the Laplace-domain transfer function of this closed loop system as:

$$H(s) = \frac{k_p s + k_i}{s^2 + s(1/\tau + k_p) + k_i} \tag{S12}$$

We first analyzed (S12) computationally by assuming different resonators for a given set of loop coefficients (solid lines in Figure 1e). We found that the resonator itself can substantially affect the system dynamics, which underlines the requirement of setting the loop coefficients for each resonator separately and carefully.

## Supplementary Note 3 Tailoring the desired system response

In this work, for oscillating a resonator at multiple of its resonant modes simultaneously, we used a dedicated PLL in closed loop with each mode. In order to track the oscillation frequency of a mode precisely, we need a flat amplitude and linear phase response in the pass-band for minimum distortion of the frequency modulation signal and high enough rejection in the stop-band for minimum cross-talk between different modes and maximum noise rejection. Hence, we shall design the PLL such that we achieve a closed-loop transfer function identical to a Butterworth low-pass filter, since it has maximally flat gain and linear phase response. Since an $n^{th}$ order Butterworth filter includes $n$ poles and no zeros in its transfer function, we start with the generalized system given in Supplementary Figure 2b utilizing an additional loop filter with $n-1$ poles in its forward path compared to the simplified model in Supplementary Figure 2a. We derived the closed loop transfer function of the system in Supplementary Figure 2b as:

$$H(s) = \frac{k_p s + k_i}{(s^2 + s/\tau)\prod_{k=1}^{n-1}(\tau_k s + 1) + k_p s + k_i} \tag{S13}$$

where $\tau_k$ are the poles introduced by the additional filter section in the forward path. Since there are one zero and $n+1$ poles in (S13), we can cancel the zero with one of the poles and position

the rest of the poles carefully to achieve an $n^{th}$ order Butterworth-type response (or similarly a Chebyshev-type or Elliptic response). We equate (S13) to a Butterworth filter transfer function with a 3-dB bandwidth, $\beta$ and solve for the unknown parameters, $k_p$, $k_i$ and $\tau_k$.

$$H(s) = \frac{k_p s + k_i}{(s^2 + s/\tau)\prod_{k=1}^{n-1}(\tau_k s + 1) + k_p s + k_i} = \frac{1}{B_n(s/\beta)} \times \frac{k_p s + k_i}{k_p s + k_i} \tag{S14}$$

where $B_n$ is the normalized Butterworth polynomial of $n^{th}$ order, which is given in [5]:

$$B_n(s) = \begin{cases} \prod_{k=1}^{\frac{n}{2}} \left[s^2 - s\ 2\cos\left(\frac{2k+n-1}{2n}\pi\right) + 1\right] & \text{if n is even} \\ (s+1)\prod_{k=1}^{\frac{n-1}{2}} \left[s^2 - s\ 2\cos\left(\frac{2k+n-1}{2n}\pi\right) + 1\right] & \text{if n is odd.} \end{cases} \tag{S15}$$

The solution of (S14) up to third order is given in Supplementary Table 1 along with the number of required poles in the additional section of the loop filter. Higher order parameters can also be calculated using symbolic toolbox of MATLAB, but the closed-form expressions are too long to be reported in this table. For loops higher than second order, the loop parameters are complex and can be implemented using digital filter design techniques. The closed loop transfer functions obtained by evaluating the calculated parameters in (S13) are given in Supplementary Figure 3.

In this work for simplicity and since the resonant mode frequencies are well separated, we implemented a first order system for driving the resonator modes using an array of PLLs. Without the need of the additional poles, the block diagram simplifies to that given in Supplementary Figure 2a. With the careful selection of the loop coefficients given in Supplementary Table 1, the system further simplifies to a first-order low pass filter with desired bandwidth.

## Supplementary Note 4 Testing the system implementation

For testing the operation of the PLL system, we first developed a z-domain model of the PLL implementation on the FPGA board. The full-scale nonlinear system implementation is given in given in Supplementary Figure 2c. For z-domain analysis we approximated the multiplier in the PLL with a subtraction operation as signals are now in the phase domain, because the multiplier and low-pass filter effectively yield the phase difference between the input and the internal oscillator. We also omit the automatic gain control, as it operates only on the amplitude of the incoming signal, and does not affect the phase. We derived the z-domain response of the CIC filter [6] as:

$$H_{CIC}(z) = \left(\frac{1}{R}\sum_{k=1}^{R} z^k\right)^N \frac{1}{R}\frac{1 - z^{-R}}{1 - z^{-1}} \tag{S16}$$

where $R$ and $N$ are the rate factor and the order of the CIC, respectively. The second term is the transfer function of a zero-order hold [4] for modeling the effect of the rate change in the CIC filter.

Similarly, the loop filter and the NCO are represented by $H_{LF}$ and $H_{NCO}$, respectively as follows:

$$H_{LF}(z) = \frac{T_S R k_i + k_p - k_p z^{-R}}{1 - z^{-R}} \tag{S17}$$

$$H_{NCO}(z) = \frac{T_S}{1 - z^{-1}} \tag{S18}$$

where $T_S$ is the sampling period of the fastest rate in the loop, which is 10 ns in this case. Note that the CIC filter and the loop filter operates at a slower rate than the NCO. Furthermore, we modeled the resonator response (S11) in z-domain as follows:

$$H_{resonator}(z) = \frac{\tau\alpha}{T_s} \frac{1 - z^{-1}}{1 + (\alpha - 1)z^{-1}} \tag{S19}$$

where $\alpha$ is $T_s/(\tau + T_s)$.

To measure the response of our PLL, we add a 10 degree phase step (a frequency pulse of about 2.7MHz for 10 ns) to the NCO and then observe the response of the NCO frequency. To ensure that our PLL implementation and its z-domain model works properly, we tested the PLL over a 9x9x3 grid of the following parameters: the proportional path gain $k_p$, the integral path gain $k_i$, and the CIC filter bandwidth, parameterized as the rate change factor, $R$. We then plot the Fourier transforms of the observed impulse responses against the predicted frequency responses from the z-domain PLL model with those particular settings, as shown for several parameter sets in Supplementary Figure 4. Then we analyzed the system with various loop coefficients with the resonator in closed loop. We found that the operation of the resonator-PLL system and the model predictions show excellent agreement.

## Supplementary Note 5 Frequency content of the particle signals

To determine the necessary bandwidth for each resonator mode, we calculate the frequency modulation signal given in [1] for a particle moving at uniform speed towards the tip of the cantilever and then returning back to the base. We then calculate the cumulative energy density for varying frequencies and determine the frequency at which 99.99% of signal energy will be retained (Supplementary Figure 5). For a 100 ms peak, these frequencies are roughly 70, 150, 185 and 210 Hz, respectively. Conservatively, we set the 3 dB bandwidth of our resonator-PLL system to a little over twice these values, yielding bandwidths of 150, 335, 435 and 505 Hz for the transfer functions shown in Figure 2b.

## Supplementary Note 6 Precision of the position estimation

We calculated the root-mean-square (RMS) error of the position estimation of a 30 fg ($\sim$ 150 nm gold) particle as a function of the position along the resonator length by using the fitting algorithm

described in the Methods section. We added experimentally measured noise waveforms to the simulated signals of identical particles passing through the resonator in 150 ms. Then, we estimated the position of each particle throughout their 150-ms transits. We calculated the RMS error of positions estimated by the fitting algorithm when the signals from first two, three and four modes as a function of particle position (Supplementary Figure 6a). The results show that the number of modes improves the precision of the position estimation.

It is known that the mass sensitivity of a mechanical resonator improves with miniaturization. In order to determine the effect of miniaturization on position precision for less dense, biologically relevant nanoparticles, we calculated the precision that could be achieved by a hypothetical SNR device utilizing a 20 $\mu$m long, 0.5 $\mu$m thick and 5 $\mu$m wide cantilever with an integrated fluidic channel (250 nm by 1 $\mu$m in cross-section). We calculate the fundamental resonant frequency of such a cantilever when it is filled with water as 1.8 MHz. Currently, our oscillator system can operate with 5 ppb frequency stability around 1.8 MHz [7]. We assumed with improved transduction techniques and high-frequency (HF) and very-high-frequency (VHF) control electronics, the same stability level could be achieved for the higher order modes as well. Under these assumptions we calculated the position precision for a human immunodeficiency virus, HIV (80-attogram buoyant mass and $\sim$100 nm size) using the same algorithm for estimating the particle position that was used for Fig. 5 of the main text. To demonstrate the effect of the increased number of modes, we expoited the first two, four and eight modes of the hypothetical SNR for the calculations. The highest frequency of operation for these three cases are 11, 61, 281 MHz, respectively. The resulting position precision is plotted in Supplementary Figure 6b.

## Supplementary References


[1] S. Dohn, W. Svendsen, A. Boisen, and O. Hansen, "Mass and position determination of attached particles on cantilever based mass sensors," *Review of Scientific Instruments*, vol. 78, p. 103303, Oct. 2007.

[2] T. R. Albrecht, P. Grtter, D. Horne, and D. Rugar, "Frequency modulation detection using high-Q cantilevers for enhanced force microscope sensitivity," *Journal of Applied Physics*, vol. 69, no. 2, p. 668, 1991.

[3] K. Kobayashi, H. Yamada, and K. Matsushige, "Frequency noise in frequency modulation atomic force microscopy," *Review of Scientific Instruments*, vol. 80, p. 043708, Apr. 2009.

[4] F. M. Gardner, *Phaselock Techniques*. Hoboken, NJ: John Wiley and Sons, 3 ed., 2005.

[5] S. Butterworth, "On the Theory of Filter Amplifiers," *The Wireless Engineer*, pp. 536–541, 1930.

[6] E. Hogenauer, "An economical class of digital filters for decimation and interpolation," *IEEE Transactions on Acoustics, Speech and Signal Processing*, vol. 29, pp. 155–162, Apr. 1981.

[7] S. Olcum, N. Cermak, S. C. Wasserman, K. S. Christine, H. Atsumi, K. R. Payer, W. Shen, J. Lee, A. M. Belcher, S. N. Bhatia, and S. R. Manalis, "Weighing nanoparticles in solution at the attogram scale," *Proceedings of the National Academy of Sciences*, vol. 111, pp. 1310–1315, Jan. 2014.